Materials & Design 264 (2026) 115745

Contents lists available at ScienceDirect

Materials & Design

journal homepage: www.elsevier.com/locate/matdes

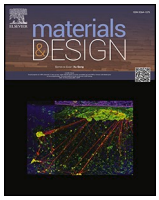

Bayesian-driven modulation of recoverable strain in compliant auxetic cementitious composites for optimal energy harvesters

Jinbao Xie [a,*], Yading Xu [b], Zhaozheng Meng [a], Minfei Liang [c], Wen Zhou [a], Yubao Zhou [a], Chen Liu [a], Erik Schlangen [a], Branko Šavija [a]

[a] Faculty of Civil Engineering and Geosciences, Delft University of Technology, Delft 2628 CN, the Netherlands
[b] College of Materials Science and Engineering, Chongqing University, Chongqing 400045, China
[c] Clarendon Laboratory, Department of Physics, University of Oxford, Oxford OX1 3PU, UK

ARTICLE INFO

Keywords:
Energy harvesting
Auxetic cementitious cellular composites
Recoverable strain capacity
Piezoelectric materials
Bayesian optimization
Concrete damage plasticity

ABSTRACT

Auxetic cementitious cellular composites (ACCCs) offer high deformability that is attractive for mechanical energy harvesting when integrated with flexible piezoelectric materials. However, the intrinsic brittleness of cement-based materials and the complex coupling between auxetic geometry and damage evolution hinder the efficient design of ACCC energy harvesters. This study proposes a novel learning-driven design framework that, for the first time, integrates a physics-based energy harvesting model with Bayesian Optimization (BO) to directly optimize the recoverable hinge-like strain capacity of ACCCs for enhanced electrical output. The optimization maximizes the voltage generated by piezoelectric materials bonded at hinge regions, while using constraints to prevent splitting failure and non-auxetic behavior under compression. The energy harvesting model combines the concrete damage plasticity (CDP) model for pre-compression damage with a secondary elastic model for cyclic loading, enabling prediction of recoverable strain in generalized ACCC geometries. The learning-driven approach proved far more efficient than random generation in identifying optimal ACCC configurations. Experimental validation of the optimized design achieved a peak-to-peak voltage of nearly 15.0 V per cycle, about 2.7 times higher than a reference design. This study provides a learning-driven approach to designing enhanced compliant auxetic cementitious energy harvesters for smart infrastructure applications.

1. Introduction

The use of fossil fuels for energy results in greenhouse gas emissions that accelerate global warming. Instead, renewable sources of energy offer a widespread and sustainable means of generating electrical energy. The renewable energy from environment sources can be harnessed effectively through the utilization of energy harvesting materials [1–5]. Piezoelectric materials are particularly effective at efficiently capturing small mechanical energies from the environment, such as human motion, vehicle vibrations, wind, and water flow. Cement-based concrete is one of the most widely used materials in infrastructure. These structures are often exposed to a variety of reciprocating mechanical loadings, such as vehicular traffic and waves [5–7]. Utilizing piezoelectricity to convert mechanical energy from cement-based infrastructures into electrical energy can supply power for lighting or sensor operations [6–8]. The addition of short fibers has transformed the properties of cementitious materials, greatly improving their tensile performance and enabling large tensile strains [9–12]. This development also facilitates the creation of cementitious materials with complex internal structures, known as Architected Cement-based Materials (ACMs) [13–16]. These ACMs demonstrate significant potential due to their superior deformation capacity, which notably enhances energy harvesting.

Auxetic cementitious cellular composites (ACCCs) exhibit outstanding mechanical performance, including high deformation capacity and enhanced energy dissipation [17–26]. Under uniaxial compression, these materials display a negative Poisson's ratio (i.e., auxetic behavior). Within the auxetic deformation range, ACCCs can sustain substantial strains and show a degree of recoverable pseudo-elastic deformation upon unloading [18–20,22,27,28]. This unique characteristic has enabled exploratory applications such as energy harvesting through the integration of piezoelectric components within ACCCs [19]. However, a systematic design approach to modulate the recoverable deformation in ACCCs for optimal energy harvesting is essential for its application across various fields. To date, the use of

* Corresponding author.
E-mail address: J.Xie-1@tudelft.nl (J. Xie).

https://doi.org/10.1016/j.matdes.2026.115745
Received 14 December 2025; Received in revised form 21 February 2026; Accepted 26 February 2026
Available online 27 February 2026

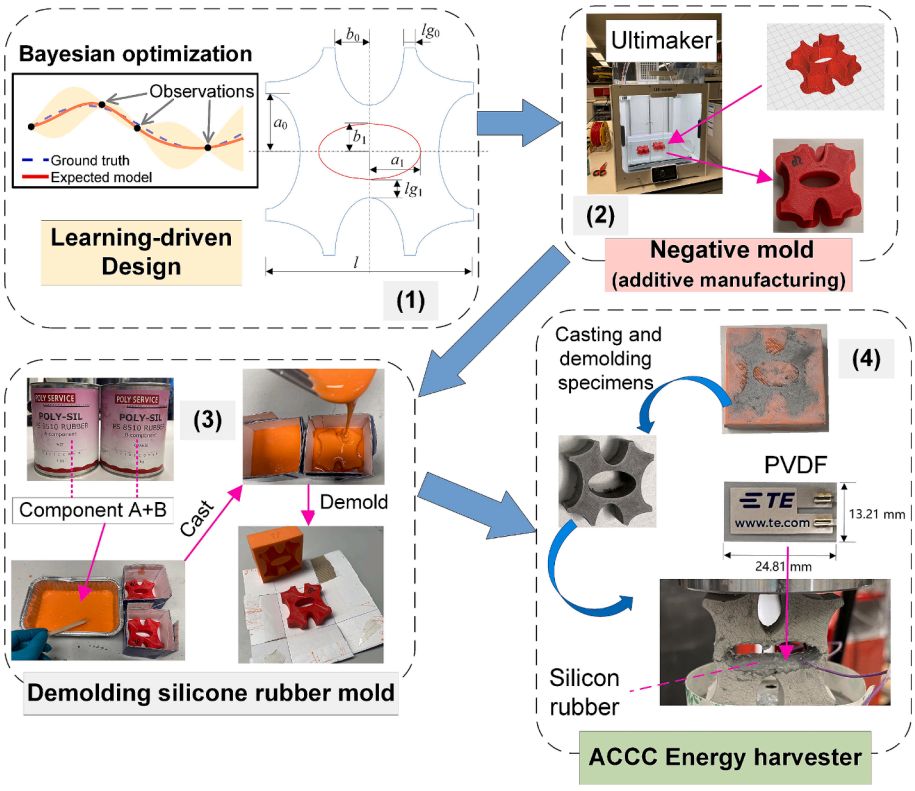

Fig. 1. Specimen fabrication of the ACCC energy harvester: (1) geometric design using active learning, (2) 3D-printed polymeric shape as a negative mold, (3) silicone rubber mold created from the 3D-printed shape, (4) casting cementitious material into the silicone mold, demolding the specimen, and bonding PVDF to fabricate the ACCC energy harvester.

auxetic materials as substrates for integrating piezoelectric components has remained limited to metallic and polymeric systems [29,30]. Recently, embedding 3D-printed polymeric auxetic reinforcement structures or other complex architected structures in cementitious mortar has increased compressive ductility, yet their recoverable deformation continues to be limited [31–39].

Unlike traditional cementitious cubes, ACCCs have complex shapes that are highly sensitive to form changes. Modifying their geometry can increase their vulnerability to damage and failure under load. Hence, optimizing their geometry for multifunctional applications poses significant challenges. Designing the intricate structure of ACCCs has so far been dependent on experimental trial-and-error methods. However, the complexity of preparing ACCC specimens, the extended curing period, and the uncertainties introduced by the heterogeneity of cementitious materials and manual casting make large-scale experimental trials both time-consuming and exhausting. Hence, modelling is essential for optimizing the performance of ACCCs. Deep learning (DL) methods have recently been explored for material design [40–45]. However, DL models generally require millions of samples or cost-function evaluations. In the case of cementitious materials, each sample—whether obtained experimentally or through finite element simulations—is computationally expensive, and evaluating the associated black-box function further increases the cost [43,44,46,47]. As a result, producing the large datasets needed for DL is not feasible, making these approaches impractical for this application.

Recently, BO has emerged as a sample-efficient and adaptive optimization method that effectively navigates large design spaces, which are challenging for traditional approaches (such as Design of Experiments (DOE)-based statistical methods [48,49], genetic algorithm [50–52]). It guides a limited number of numerical models toward highly probable optimal results while generating surrogate models that describe the properties of interest based on the design variables [53–58]. Bayesian approach has been employed to optimize mechanical properties of lattice configurations made from polymeric materials [59,60]. However, no research has used BO in any ACMs, including ACCCs, to date. ACCC models face challenges in modelling for dataset creation and optimization. These challenges stem from the brittleness of cementitious matrix, as well as complex topologies and contact boundary conditions.

This study introduces a learning-driven computational framework to achieve optimial design for ACCC energy harvesters. The framework integrates an energy harvesting model with BO to maximize the recoverable strain in ACCCs, thereby enhancing the output voltage of piezoelectric materials bonded to the hinge-like ligament region. Constraints are applied to eliminate designs that exhibit splitting or non-auxetic behavior under compression during BO process. The optimized shape was experimentally tested for output voltage. Geometric and mechanical evolution during BO iterations were further investigated, offering insights for high-performance design of ACCC energy harvesters.

2. Experiments

2.1. Materials and specimen preparation

The fabrication of ACCCs followed the “indirect printing” process [17], as shown in Fig. 1. First, a unit cell with specific dimensions was designed and produced using Fused Deposition Modeling (FDM) with a 3D printer (Ultimaker S5). ABS was selected as the printing material. The printed ABS structures were then placed inside a cardboard box. Next, a two-component silicone rubber, Poly-Sil PS 8510, was mixed in a 1:1 mass ratio and poured into the box. The silicone rubber was left to cure at room temperature for at least one hour until it hardened. Once solidified, the silicone rubber was removed from the box to be used as a mold for casting the cementitious materials. Herein, 8510 silicone rubber, with a Shore hardness of 10 A, provides adequate stiffness for use as a mold while maintaining the flexibility needed for easy demolding. The

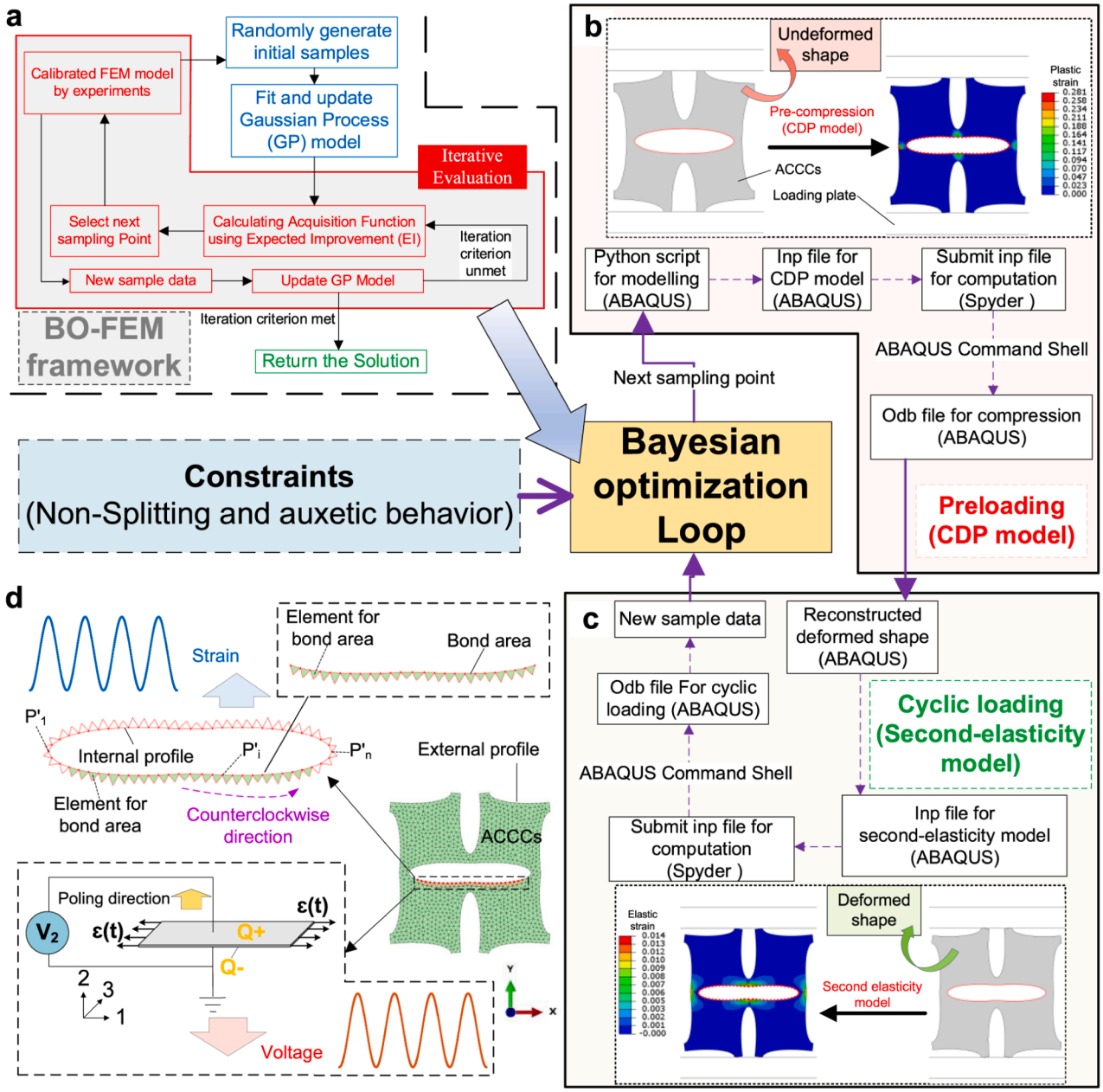

Fig. 2. An overview of the proposed computational BO-FEM active learning framework, (a) the BO algorithm interactively queries the FEM to propose new design with high potential to enhance the objective function, (b) the CDP model in ABAQUS was utilized for pre-compression in each BO loop, interacting with the BO agent Spyder, (c) the second-elasticity model in ABAQUS was utilized for cyclic loading in each BO loop, interacting with the BO agent Spyder, (d) the average strain $\bar{\varepsilon}_{int}$ of the cementitious material bonded to the PVDF film is calculated as the objective function to maximize the voltage output based on piezoelectric formulations.

mix design, processing, and additional sample preparation details of the cementitious materials are provided in Supplementary Section 1.

A piezoelectric film, Polyvinylidene Difluoride (PVDF), was bonded around the ligament region of the central elliptical hole in the specimen using silicone rubber (Poly-Sil PS8540) and allowed to cure for at least 12 h until fully hardened. This is because 8540 silicone rubber, with a Shore hardness of 40 A, provides good bond strength. The LDT0-028 K PVDF film measures 24.81 mm × 13.21 mm with a total thickness of 0.2 mm, which includes a protective layer designed to prevent surface oxidation of the silver ink electrode area [7,61,62]. The piezoelectric layer within the PVDF film has a thickness of 28 μm. To reduce strain transfer loss from the bonded ligament area to the PVDF during pre-compression, the PVDF film was bonded to the ligament region after precompression. The bonding was performed when the silicone rubber (Poly-Sil PS8540) had lost its fluidity and exhibited strong adhesive properties, approximately one hour after mixing its components A and B.

2.2. Experimental setup

Material properties were characterized through uniaxial tensile and compression tests (see Supplementary Section 2). Cyclic testing of the energy harvester was conducted using an MTS fatigue machine with a 10 kN capacity. The harvester's DC output voltage was measured with a Keysight 34,461 A digital multimeter (DMM). Two wires connected the PVDF to the multimeter, and a plastic film reduced friction between the loading plate and the specimen. To mitigate slight horizontal movement caused by uneven deformation and asymmetrical cracks in the cementitious materials during cyclic tests, tape was applied to the edges of the bottom loading plate. The energy harvesting test setup and loading plan for the ACCC energy harvester are shown in Supplementary Section 3.

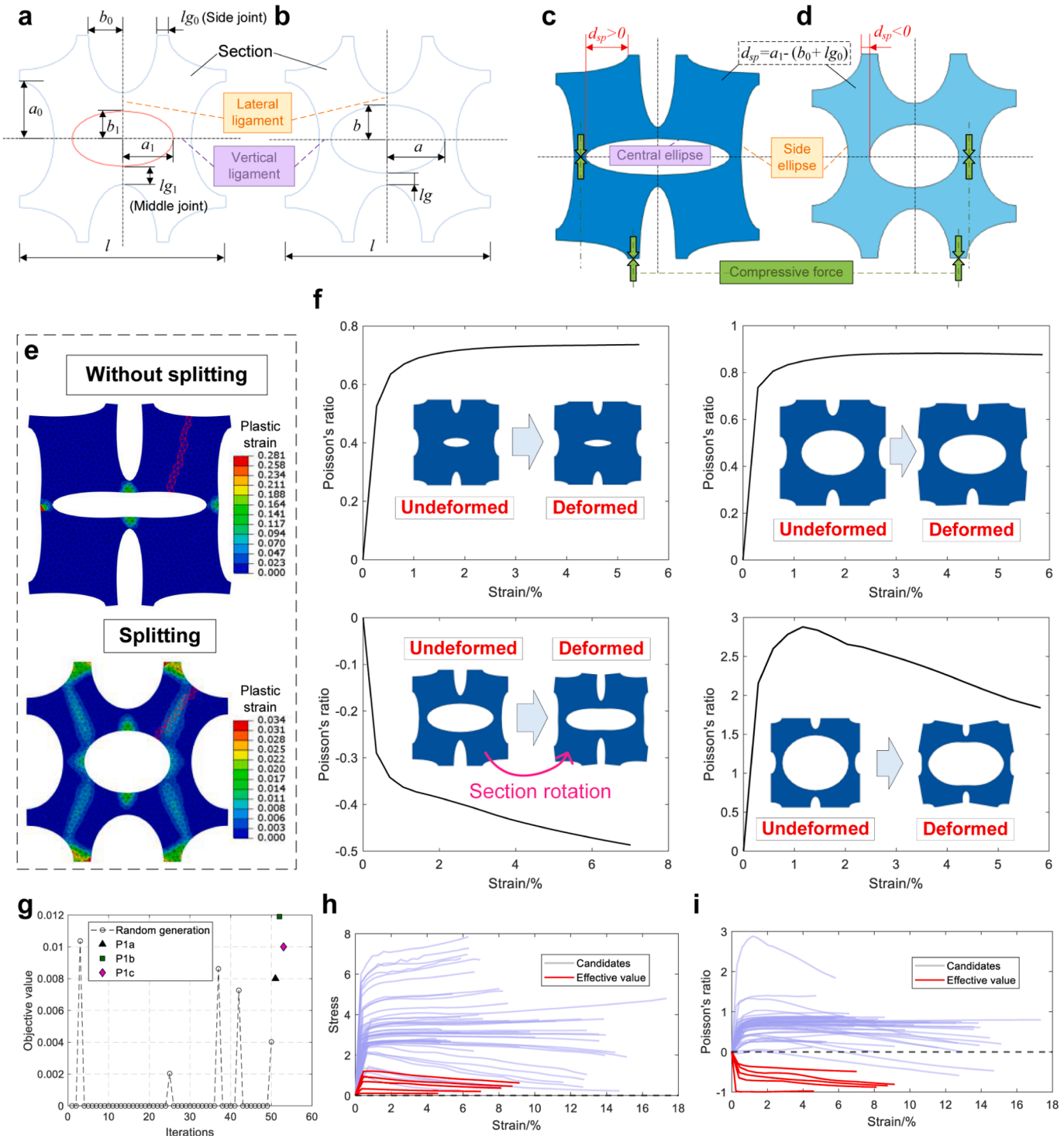

Fig. 3. Parameterization of ACCCs with constraints. (a) geometric parameterization of ACCCs, (b) ACCCs shape with identical ligaments, (c) ACCCs shape with larger d_{sp}, (d) ACCCs shape with smaller d_{sp}, (e) splitting case identified by plastic strain in detection region, (f) four randomly generated samples with different Poisson's ratios, (g-i) results of random generation: objective values (g), stress–strain curves (h), Poisson's ratio (i).

3. Learning-driven computational framework for optimization

A learning-driven framework was developed by utilizing the interaction between a FEM-based energy harvesting model and BO to optimize hinge-like recoverable strain capacity in ACCCs. This strain capacity optimization maximizes the output voltage of piezoelectric materials bonded to the hinge-like ligament region, according to the piezoelectric model described in Supplementary Section 4. The technical workflow of the BO-FEM framework is illustrated in Fig. 2a. Using the initial sample data, a new geometric parameterization of ACCCs with the highest probability for improving the objective value is (i) selected by BO, (ii) its geometry is generated, (iii) its objective value (i.e., recoverable strain $\bar{\varepsilon}_{\text{int}}$) is calculated using FEM, and (iv) Gaussian probabilistic models of the quantity of interest ($\bar{\varepsilon}_{\text{int}}$) are updated after each evaluation considering the constraints. This iterative process continues until convergence is reached, where no significant improvement is

observed in the best objective value. During the optimization process, the current best objective value, geometric parameters, and mechanical performance (including Poisson's ratio and the stress–strain curve) are recorded. Fig. 3a shows the geometric parameterization of elliptical-shaped ACCCs for a sample point (i.e., $\mathbf{x}_i = (l_i, a_{0i}, b_{0i}, a_{1i}, b_{1i})$). The central hole is considered to potentially differ from the surrounding holes in the unit cell. The initial step involves assuming that the central hole has the same size as the surrounding holes in the unit cell (see Fig. 3b). This special case is followed by adjustments to the dimensions of the central hole. Considering the limited space for casting cementitious materials that include fibers, the minimum specified value for the ligament $lg_{\min}$ is set at 3.5 mm.

In each BO-FEM loop, the energy harvesting model of ACCCs comprises two phases: preloading and cyclic loading. In the pre-compression phase, the CDP model quantifies ACCCs' mechanical behavior [8], as shown in Fig. 2b. See more details in Supplementary Section 2 for the calibration of the CDP model. ACCCs display recoverable pseudo-elastic deformation after compressive unloading in cyclic tests, attempting to return to their original shape despite minor plastic deformation [17–20]. However, due to its limitations, the CDP model encounters difficulties in simulating the recoverable deformation elasticity during cyclic loading. To address this, a second-elasticity model (Fig. 2c) was utilized instead. This model captures the recoverable deformation elasticity by representing the unit cell's overall elastic behavior with an equivalent structural elastic modulus during cyclic loading [19]. For transition between models, the ACCCs' deformed shape at a specified loading displacement (calculated by the CDP model) is set as the initial geometry for the second-elasticity model by using an improved node-order-track algorithm for ACCC shape topology reconstruction (see Supplementary Section 5). The FEM model was implemented in the ABAQUS and connected via a developed interface to Spyder, where BO optimization was executed. As seen in Fig. 2d, the average strain $\bar{\varepsilon}_{\text{int}}$ of the cementitious material bonded to the PVDF film is treated as our objective function to simplify the representation of the output voltage. To calculate $\bar{\varepsilon}_{\text{int}}$, 80% of the bottom region of the internal profile in each ACCCs shape was designated as the bonding area through node editing algorithm (Supplementary Section 6). In this study, $\bar{\varepsilon}_{\text{int}}$ is employed as a comparative surrogate metric within the optimization framework rather than as a direct predictor of absolute voltage output. In practice, mechanisms such as adhesive debonding, imperfect strain transfer, cementitious crack-path variability, and cementitious material heterogeneity may partially decouple $\bar{\varepsilon}_{\text{int}}$ from the measured piezoelectric response. Accordingly, $\bar{\varepsilon}_{\text{int}}$ is used to rank relative performance trends within the explored design space, while absolute voltage levels remain influenced by interfacial and material factors beyond the present modeling scope. Further work will aim to better quantify this relationship through expanded multiphysics modeling and experimental validation.

For each generated shape, the applied displacement in the CDP model was only considered up to the smaller value between b_0 and b_1. Therefore, the contact between the top and bottom ends of the central elliptical hole (i.e., self-contact within this hole) is not considered, nor is the contact at the side joints in the section due to rotation. This is because ACCCs tend to split when these contacts occur, as their negative Poisson's ratio decreases under compression. Previous experiments revealed that when the compressive displacement approaches half the size of the compressible hole, the ligament accumulates significant plastic deformation and damage, leading to a further reduction in recoverable deformation [20]. For smaller ligaments, this poses a higher risk of failure. Therefore, the deformation shape after a compressive displacement equal to one-quarter of the hole size (i.e., half of the smaller value between b_0 and b_1.) was uniformly selected as the initial geometry for each candidate in the secondary elastic model. In the second elastic model, the applied displacement amplitude for each shape is set to 10% of the smaller value between b_0 and b_1.

The geometric parameter d_{sp} in Eq. (1), representing the degree of structural chirality, was introduced to characterize the splitting behavior of ACCCs. As illustrated in Fig. 3c, a higher d_{sp} increases the lateral distance between the side joints and middle joints. This adjustment reduces the compressive force (highlighted by the green arrow in Fig. 3d) required to create the moment necessary for ligament plastic deformation and subsequent section rotation, thereby promoting the development of a negative Poisson's ratio effect. Conversely, the ACCCs shape depicted in Fig. 3d is less conducive to auxetic behavior and is prone to splitting due to the increased compressive force exerted on the joints.

$$d_{sp} = a_1 - (b_0 + lg_0) \tag{1}$$

The input geometric parameter was restricted to a specific size range, with intra-point constraints applied to these input-dependent geometric parameters, as detailed in Supplementary Section 7. Additionally, output constraints (black box constraints) were applied to eliminate cases of splitting failure (Removed case (i) in Fig. 3e) and non-auxetic behavior (Removed case (ii)) under compression, as these are unsuitable for energy harvesting. This was imposed on the objective value of each individual candidate by multiplying it by zero in two specific cases that needed to be removed. The multiplier applied to the objective value was determined through trial and errors, allowing the BO process to avoid these points without hindering the exploration of candidate points by the acquisition function. Experimental details can be found in Supplementary Section 8 for the splitting behavior in Removed case (i). To better illustrate Removed Case (ii), Fig. 3f presents four randomly generated ACCC candidates with different Poisson's ratio-strain curves under compression. It was observed that only the bottom-left subfigure in Fig. 3f exhibits a negative Poisson's ratio.

50 parameterizations were randomly generated, and those with non-zero objective values were selected. Fig. 3g-i show the distribution of these objective values and their stress–strain curves and Poisson's ratio-strain curves, where only 5 out of the 50 parameterizations had non-zero objective values. This indicates the inefficiency of using randomly generated data for optimization. This inefficiency arises from the quasi-brittle nature of cementitious materials, as modifying the geometry of ACCCs can increase their susceptibility to damage and splitting failure under load. Additionally, the intricate shapes of ACCCs are highly sensitive to geometric changes aimed at enhancing recoverable hinge-like strain capacity while maintaining auxetic behavior. Furthermore, ACCCs initially form small cracks under compression due to the strong fiber-bridging capacity of SHCC, requiring a refined specification of geometric parameters. This, in turn, expands the design space and leads to an exponential increase in computational cost. In Fig. 3g, the three ACCC shapes designed as intuitive solutions (including the reference P1a) are compared to the randomly generated shapes regarding their objective values. Details of the three intuitive solution designs are provided in Supplementary Section 2.

As a sample-efficient optimization strategy, BO can identify optimal objective values using only a small amount of initial data [55,56,59,60]. For the dataset generated through random generation, the objective values were manually penalized instead of being directly derived from the model results. This approach may cause challenges in identifying non-zero acquisition function values in BO, thereby hindering the acquisition function from effectively guiding the exploration of the design space. Therefore, the 5 non-zero values were combined with the three previously used parameterizations to form the initial dataset for subsequent optimization. The optimizations were performed sequentially, with a batch size of one, to maximize the performance of BO [63]. Although BO is inherently a sequential algorithm, it can be adapted to execute multiple optimizations simultaneously, updating the surrogate model only after all evaluations are completed [64]. While this parallel approach can save considerable time, it typically results in less effective optimization outcomes within a fixed number of trials. Expected Improvement (EI) [65] was employed as the acquisition function in BO to estimate the potential improvement over the current best observation

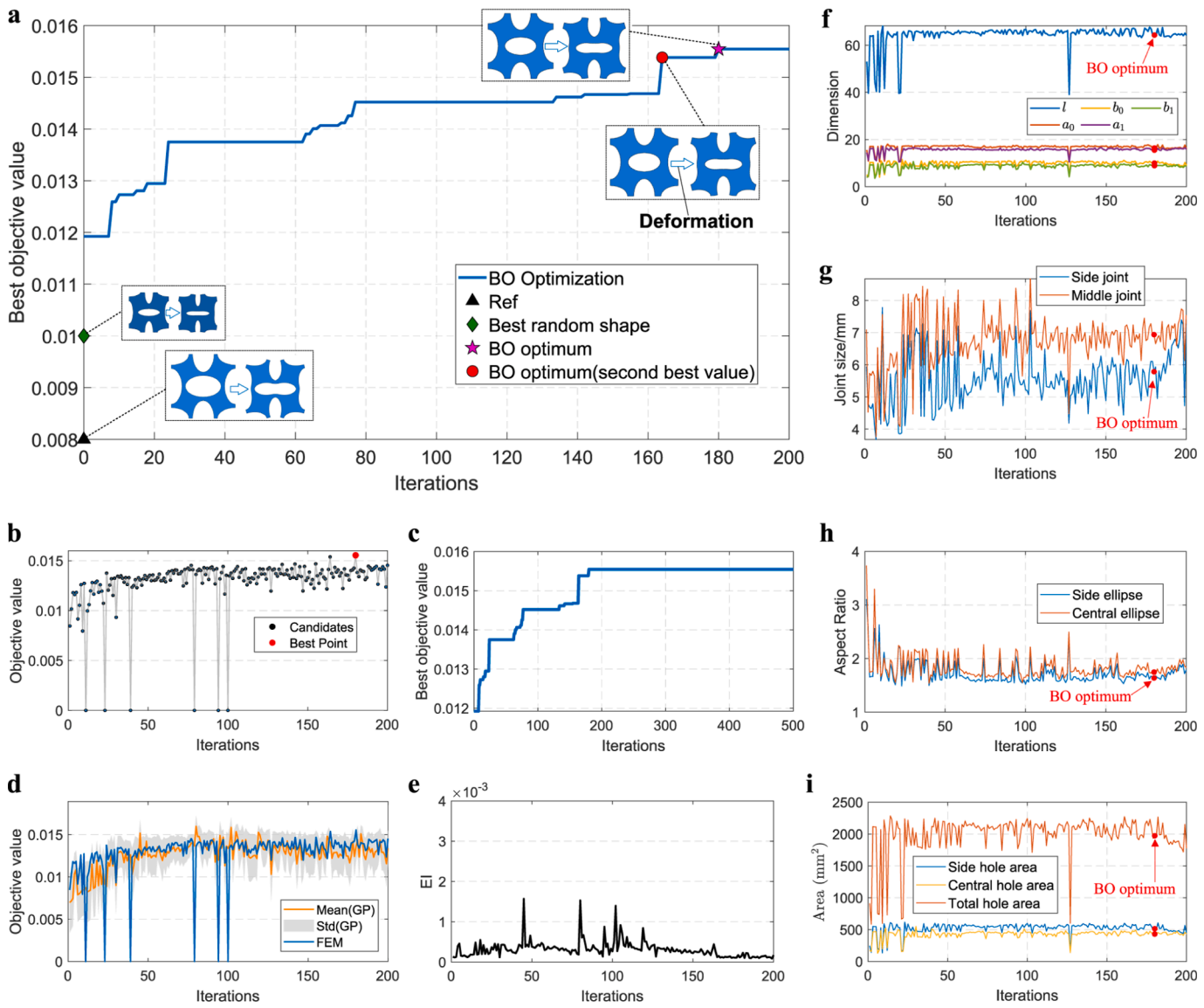

Fig. 4. Convergence of BO: (a) FEM-evaluated best objective value (with insets showing the initial shape and corresponding deformed shape for cyclic loading), (b) progression of FEM-evaluated objective values, (c) FEM-evaluated best objective value until 500 iterations, (d) comparison between GP surrogate predictions and FEM-evaluated objective values over iterations, with the shaded region showing the standard deviation of GP prediction, (e) evolution of EI, (f) absolute geometric dimensions of the ACCC unit cell versus iteration number, (g) variation of joint sizes throughout the optimization process, (h) aspect ratios of the side and central elliptical holes versus iteration number, (i) evolution of hole areas, including side hole area, central hole area, and total hole area, throughout the BO process.

at each sample point (see more details in Supplementary Section 9). It balances exploration of design space regions with high uncertainty (exploring new areas) and exploitation of regions with potentially high objective function values (refining known promising areas) to guide the selection of the next point for evaluation. Since solution quality was the primary focus of this study, BO was conducted in a purely sequential manner.

4. Results and discussion

4.1. Optimization results

Fig. 4 illustrates the BO process in searching for the optimal objective value. In each iteration, a candidate is proposed by the BO acquisition function and evaluated using the FEM to obtain its objective value, along with the current best value throughout the optimization process (Fig. 4a). Fig. 4b presents the objective value of each candidate evaluated by FEM at every iteration. As shown in Fig. 4a, the reference shape (Ref in Fig. 4a), P1a, exhibits a low $\bar{\varepsilon}_{int}$ of 0.008. For the randomly generated shapes, the best configuration only reached a $\bar{\varepsilon}_{int}$ of 0.01 (Best random shape in Fig. 4a), which is higher than the reference. In contrast, during the BO process, the best objective value $\bar{\varepsilon}_{int}$ exhibited a general trend of improvement over iterations. In the first 80 iterations, the best objective value increases rapidly, after which it slowly improves and eventually converges. The best shape optimized through BO at iteration 180 achieves a $\bar{\varepsilon}_{int}$ of 0.0155 (BO optimum in Fig. 4a), nearly twice the objective value of the reference shape. Notably, the best value obtained at iteration 180 offers only a marginal improvement over the second-best value achieved at iteration 164 (second-best BO optimum in Fig. 4a). In Fig. 4b, there were only six candidates where the objective value dropped to zero due to predefined artificial constraints, indicating violations of the criteria for non-splitting and auxetic behavior. This further highlights the efficiency of BO compared to random generation methods in optimization. It is worth noting that not every iteration led to improvement, as BO balances exploiting high-performing regions with exploring new possibilities. This is reflected in the progression of the

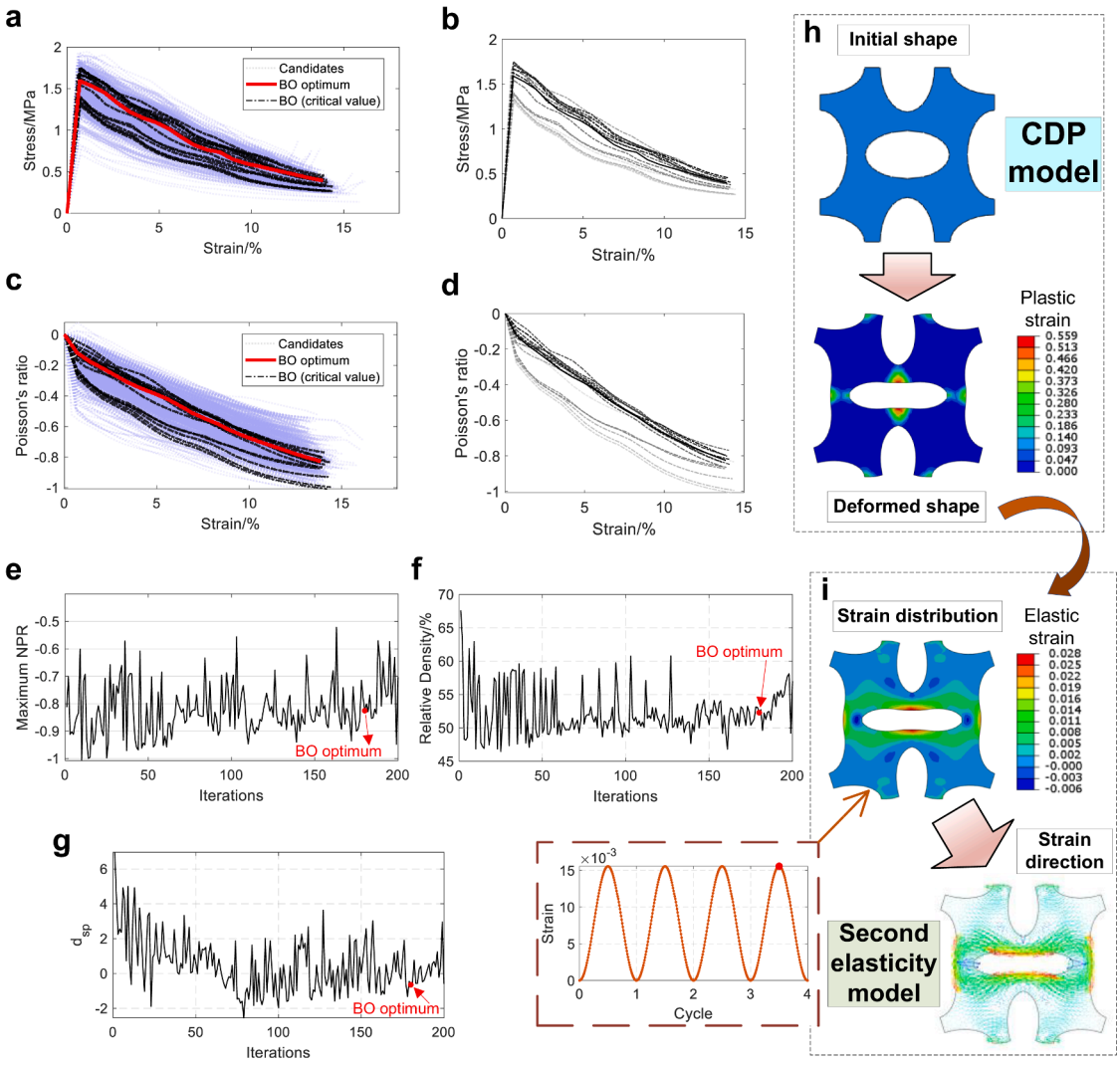

Fig. 5. Mechanical performance evolution of BO during iterations, (a) stress–strain curves of all sampled candidate designs during optimization, with the BO-identified optimum and the best-so-far (critical) candidate design highlighted, (b) stress–strain responses of the selected critical candidate designs, (c) evolution of Poisson's ratio with strain for all candidates during optimization, with the BO-identified optimum and the best-so-far (critical) candidate design highlighted, (d) poisson's ratio–strain curves of the critical candidate designs, (e) evolution of the maximum negative Poisson's ratio (NPR) achieved by each design over BO iterations, (f) variation of the unit-cell relative density during optimization, (g) evolution of the splitting-related parameter (d_{sp}) over BO iterations, (h) CDP model of ACCCs shape (BO optimum) showing plastic strain distribution under pre-compression, (i) second elasticity model of ACCCs shape (BO optimum) showing elastic strain distribution and principal strain directions during cyclic deformation.

objective value throughout the BO process in Fig. 4b. The process achieved rapid optimization during the first 100 iterations, marked by significant fluctuations due to exploration. After 100 iterations, fluctuations diminished as the focus shifted to refinement. By 200 iterations, the best objective value remained unchanged through 500 iterations (Fig. 4c), indicating convergence of the optimization process and that a near-global optimum had been attained. To ensure computational efficiency, only the results from the first 200 iterations were used in the subsequent analysis.

For each candidate design in Fig. 4d, the GP surrogate model provides a predictive mean and associated uncertainty (standard deviation), represented by the orange curve and the grey shaded band, respectively. The corresponding objective values obtained from FEM of the same candidates are shown by the blue curve (corresponding to the objective values of the candidates in Fig. 4b). The comparison between the surrogate predictions and the FEM evaluations illustrates the learning behavior of BO and the progressive refinement of the surrogate model over successive iterations. As the iterations proceed, the discrepancy between the GP mean prediction and the FEM evaluation becomes smaller, and the predictive uncertainty gradually narrows, demonstrating that the surrogate model is being refined as more data points are incorporated. The FEM curve and the BO mean curve show increasingly consistent trends after approximately 100 iterations, suggesting improved surrogate accuracy and stability. Overall, the progressive convergence behavior of BO demonstrates that GP effectively models the objective function and, with the support of EI, identifies candidates with near-optimal objective values. These fluctuations in the GP are a natural consequence of BO, which explores promising regions with high predictive uncertainty to identify the optimal solution, occasionally leading to temporary variations in predictive performance as new informative samples are incorporated across iterations. Additionally, the complexity of the energy harvesting model and predefined artificial constraints may contribute to variability. Overall, the GP surrogate model maintains strong predictive performance throughout the optimization, as further detailed in Supplementary Section 10. Fig. 4e further illustrates the evolution of the EI acquisition function over the optimization iterations. Higher EI values appear mainly in the early stages, promoting exploration of the design space. As the optimization converges, EI gradually

decreases, reflecting reduced uncertainty and a shift toward exploitation near the optimal region. A near-zero EI at later stages indicates that the optimization process has effectively converged. During the search for the optimum, BO actively explores promising regions with high predictive uncertainty in the GP surrogate through the acquisition function, which leads to pronounced EI fluctuations (Fig. 4e). Some of the sampled candidates, however, have FEM-evaluated objective values of zero, due to predefined artificial constraints.

The dimensions of the five design variables (Fig. 4f) exhibit relatively rapid fluctuations during nearly the first 50 iterations. These are followed by smaller fluctuations as the values gradually stabilize near their optimal levels. It is evident that $a_0 > a_1$, $b_0 > b_1$. This progression indicates that the elliptical hole shape gradually transitions toward a circular form, with an increase in the lateral distance (b_0) between the two side joints in contact with the loading plate. As b_0 increases, a higher compressive load is required to achieve the same moment necessary for the ligaments to undergo plastic deformation and result in section rotation, assuming the constitutive materials have identical tensile strength. At the same time, the increased frictional force at the loading joints induces greater tensile force in the ligaments, as dictated by force equilibrium. This, in turn, leads to the formation of larger cracks in the ligaments, ultimately contributing to a higher objective value.

In Fig. 4g, both the side and middle joint sizes increase with significant fluctuations during nearly the first 100 iterations before stabilizing with diminished variations. This occurs because larger joints produce greater crack openings at the same rotation angle and increase compressive force due to higher bending resistance, which, in turn, raises frictional force at the loading joints and induces greater tensile force in the ligaments. In Fig. 4h, the aspect ratios of both the side ellipse and central ellipse (denoted in Fig. 3) keep decreasing in the initial 50 iterations with significant fluctuations and stabilize after 50 iterations with decreasing fluctuations. This trend also indicates that the elliptical hole shape gradually transitions into a circular form, causing more pronounced cracking in the ligaments, as explained in Fig. 4f. In Fig. 4i, the hole areas show significant fluctuations in the early iterations, followed by a slight decrease. Supplementary information related to Fig. 4 is presented in Supplementary Section 11. This section also includes the critical candidates corresponding to the best-so-far objective values in Fig. 4a, which were selected for analysis and reordered according to their sequence in BO process. These points indicate improvements over the previous best objective values during BO iterations.

Fig. 5 shows the mechanical performance evolution during BO iterations. Fig. 5a displays the stress–strain curves of all candidates, with critical candidates mainly clustering in the upper-middle region and exhibiting relatively higher peak stress. This clustering occurs because lower curves with reduced peak stress are associated with smaller joint sizes, higher hole aspect ratios, and lower relative densities, which limit the formation of large crack regions to improve the objective function. As the curves shift upward with increasing peak stress, larger cracks develop at the ligaments. However, excessive ligament size eventually leads to splitting behavior, which BO mitigates using penalty constraints. Fig. 5b shows the stress–strain curves of the best-so-far (critical) candidates, with color intensity indicating iteration progress. As iterations advance, the curves move upward (from lighter to darker colors) with increasing peak stress, reflecting larger joint sizes, reduced hole aspect ratios, and higher relative densities. These changes facilitate greater crack formation in the ligaments, improving the objective function. However, the optimized curve is not the one with the highest peak stress (solid line in Fig. 5b), suggesting that additional factors influence the objective function. Fig. 5c illustrates the variation in Poisson's ratio during compression for all candidates, with the critical candidates mainly clustering in the middle region. Fig. 5d shows the Poisson's ratio variation for these critical candidates, with color intensity indicating iteration progress. As iterations advance, the curves shift upward (from lighter to darker colors), reflecting a lower absolute value of negative Poisson's ratio, which suggests larger joint sizes, reduced hole aspect ratios, and higher relative densities. These changes also facilitate greater crack formation in the ligaments and thus improve the objective function. However, the optimized curve does not correspond to the one with the lowest absolute value of negative Poisson's ratio (solid line in Fig. 5d), indicating the influence of additional factors on the objective function. Furthermore, the magnitude of negative Poisson's ratio (denoted as Maximum NPR in Fig. 5e) shows a slight decrease with some fluctuation due to the balance between exploration and exploitation during BO iterations. In Fig. 5f, the relative density of the critical candidates continues to increase, with some minor fluctuations. Correspondingly, the reduction in hole area in Fig. 4i indicates an increase in material volume (i.e., higher relative density), resulting in larger joint sizes and more pronounced cracking. This benefits the objective function if non-splitting and auxetic behavior are maintained.

Similarly, as d_{sp} decreases, the structural chirality diminishes. This reduction requires the ligaments (illustrated in Fig. 3) to withstand higher externally applied compressive stress to achieve section rotation, leading to the development of larger cracks in the ligaments. The parameter d_{sp} decreases over iterations in Fig. 5g, although with some fluctuations, but finally tend to be fluctuate around zero where the optimum point is located. When d_{sp} is negative, that means vertical ligaments are subjected to more compressive force, which may result in local compressive failure locally and further develops to splitting failure. However, this progression eventually results in a condition closer to splitting failure, causing the objective value to drop to zero due to the constraints imposed by BO. Therefore, BO seeks to avoid this situation and focuses on identifying points that fluctuate around a zero value for d_{sp} to find the optimal solution. The condition $d_{\mathrm{sp}} > 0$ is not imposed as an explicit constraint in the optimization. Instead, splitting failure is indirectly penalized by monitoring the plastic strain within the central detection region. The convergence of d_{sp} toward values near zero therefore reflects its physical correlation with compressive splitting behavior rather than boundary saturation of a prescribed constraint. In this context, d_{sp} may be interpreted as an emergent indicator associated with failure, rather than a directly constrained design variable. While the results suggest that avoiding negative d_{sp} may help mitigate splitting failure within the explored design space, detailed mechanical mechanisms linking structural chirality, d_{sp}, and failure evolution need further investigation.

Furthermore, Fig. 5h shows the CDP model of the optimized candidate (BO optimum in Fig. 4a), which demonstrates a larger plastic strain and a more extensive plastic zone in its deformed shape under compression compared to the reference in Fig. S7. In Fig. 5i, the optimal design exhibits greater elastic strain and a more extensive tensile zone near the ligaments at the peak point of $\bar{\varepsilon}_{\mathrm{int}}$ during cyclic loading in the second elasticity model, compared to the reference in Fig. S7. The highest elastic strain is concentrated at the middle joints, with tensile strain indicated in the strain direction. In Fig. 5i, $\bar{\varepsilon}_{\mathrm{int}}$ exhibits a sinusoidal curve during cyclic loading, with a peak value of 0.0155. Supplementary information related to Fig. 5 is presented in Supplementary Section 11.

The BO results indicate that the electromechanical performance of ACCC-based energy harvesters is governed by coupled geometric effects rather than monotonic variation of any single parameter. To mitigate splitting failure, the splitting-related parameter d_{sp} requires careful consideration. Within the investigated parameter range, decreasing d_{sp} is associated with reduced structural chirality, weakened auxeticity, and increased ligament cracking, which may increase the likelihood of splitting under compression. In addition, moderately reducing joint size, increasing the hole aspect ratio, and decreasing the relative density can further mitigate splitting risk, particularly when fiber-bridging capacity is limited. Once splitting failure is effectively suppressed and auxetic behavior is preserved, the energy harvesting performance can be enhanced through controlled geometric tuning. Specifically, moderately decreasing d_{sp}, increasing joint size, reducing the hole aspect ratio, and increasing relative density promote stable hinge-like deformation and

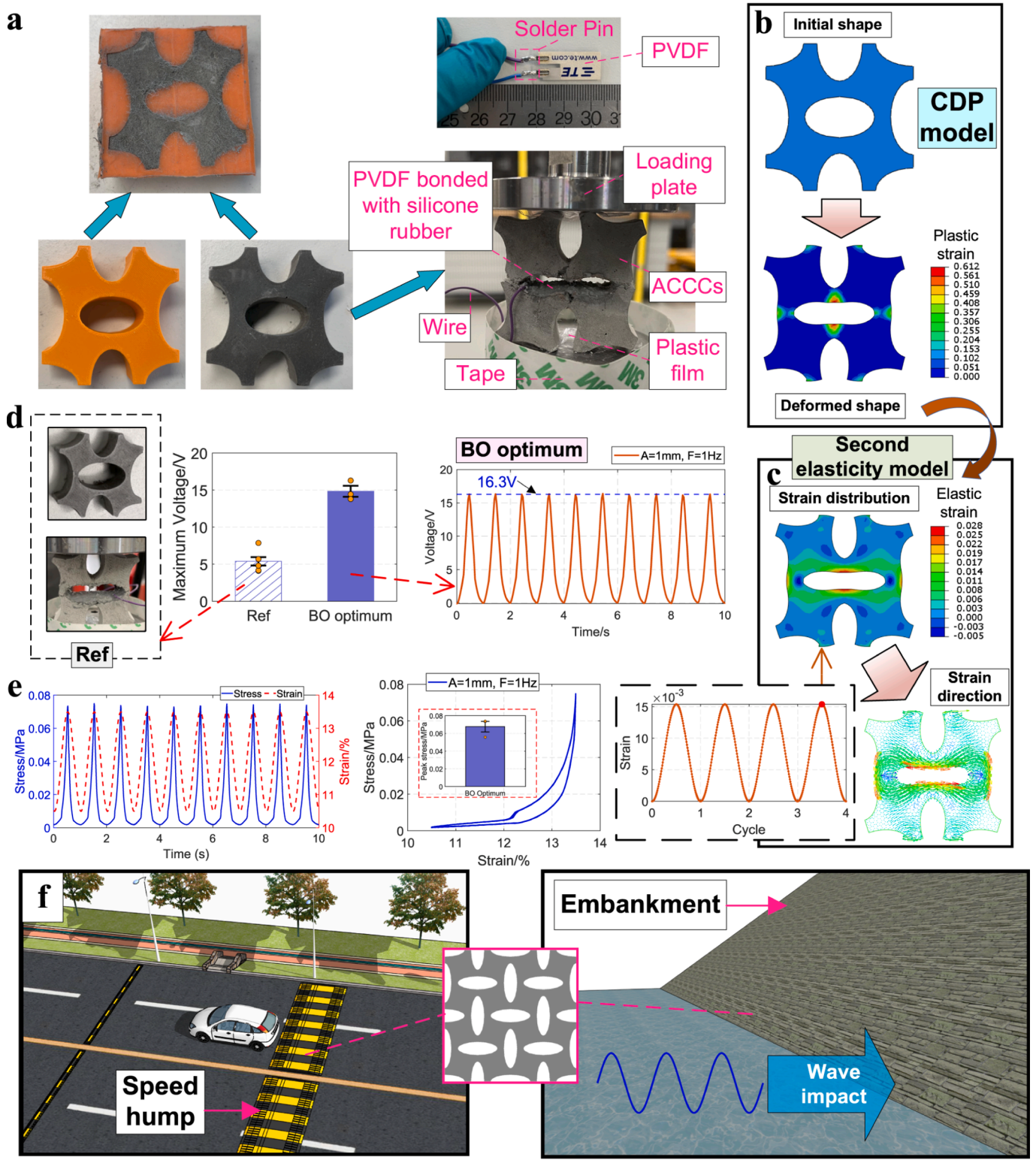

Fig. 6. Experimental validation, (a) sample preparation and energy harvesting test setup of optimized ACCC shape, (b) CDP model of optimized ACCC shape, (c) ε_{int} of optimized ACCC shape and its second elasticity model, (d) Output voltage of optimized ACCC shape during energy harvesting test (error bars represent the standard deviation, and orange markers denote results from individual tests, illustrating data scatter), (e) stress–strain curve of optimized ACCC shape during energy harvesting test, (f) potential applications of the energy harvester. (For interpretation of the references to colour in this figure legend, the reader is referred to the web version of this article.)

more effective strain transfer to the bonded piezoelectric layers, thereby increasing voltage output. However, a fundamental trade-off exists between structural robustness and electromechanical efficiency, as geometric modifications that improve electrical output may simultaneously elevate splitting risk if auxeticity is weakened. Therefore, optimal design requires balancing splitting resistance, auxetic response retention, and strain transfer efficiency, and should be validated through combined numerical and experimental approaches.

4.2. Experimental validation

Considering the PVDF size and the solder pin length, the second-best shape from BO ("BO Optimum (Second Best Value)" in Fig. 4a) was chosen for experimental validation, as shown in Fig. 6. This shape has a $\bar{\varepsilon}_{\text{int}}$ of 0.0154, very closely matching the 0.0155 of the best shape (BO optimum in Fig. 4a). Fig. 6a depicts its manufacturing process and the energy harvesting experimental setup for the optimized shape. Fig. 6b displays the CDP model of the optimized shape, which demonstrates similar plastic strain and plastic zone characteristics in its deformed state under compression, comparable to those of the best shape ("BO Optimum" in Fig. 4a). Fig. 6c also shows similar elastic strain distribution and strain direction for its deformed shape at the peak point of $\bar{\varepsilon}_{\text{int}}$ during cyclic loading in the second elasticity model. The highest tensile elastic strain, concentrated at the middle joints, follows a sinusoidal pattern during cyclic loading, with a peak value of 0.0154.

During energy harvesting test, the second-best shape is initially compressed by displacement loading, starting from zero and increasing to U (8.0 mm), resulting in a deformed specimen height of nearly 59 mm. Considering the thickness of the silicon rubber layer, further compression could cause contact between the upper and lower ends of holes. Subsequently, cyclic loading is applied under displacement control, utilizing a sinusoidal wave with a constant amplitude A (1 mm) and a frequency f (1 Hz). The energy harvesting test results of ACCCs for the second-best shape based on three replicate specimens are presented in Fig. 6d and Supplementary Movie 1. This depicts a sinusoidal output voltage with a peak-to-peak value of 14.8 ± 0.8 V per cycle of cyclic loading (mean ± standard deviation), showcasing nearly 2.7 times higher than the reference shape (P1a). Details of the energy harvesting results of the reference one are provided in Supplementary Section 3. Fig. 6e presents the dynamic stress–strain curve of the second-best shape obtained from three replicate specimens during the energy harvesting test, with a peak stress of 0.0677 ± 0.0060 MPa (mean ± standard deviation). Additional comparisons between optimized ACCC shapes and the reference are provided in Supplementary Section 12. The experimental validation is limited to a comparison between the optimized geometries and the reference geometry. Accordingly, the experimental evidence supports a comparative assessment within this specific subset of designs rather than a comprehensive generalization across the entire design space. Future studies will include experimental validation of additional geometries spanning wider ranges of structural parameters to further examine the robustness and generalizability of the proposed framework.

Fig. 6f illustrates potential applications of ACCC energy harvesters for powering smart infrastructure systems. For example, ACCC energy harvesters could be embedded in speed humps to capture energy from vehicle-induced impacts, or deployed in coastal areas to harvest kinetic energy from ocean wave loading. However, infrastructure-scale deployment of such systems remains conditional and will require careful consideration of the limitations identified in the present study. In particular, fatigue resistance under repeated loading, long-term mechanical durability, and circuit load matching were not systematically evaluated here. Therefore, further investigation is necessary to validate long-term reliability and practical feasibility before large-scale implementation can be realized, as discussed in the Conclusions and Supplementary Section 13.

5. Conclusions

This study introduces a learning-driven computational framework to achieve optimial design for ACCC energy harvesters. The optimized results were validated through energy harvesting experiments, demonstrating a peak-to-peak value of approximately 15 V per cycle of cyclic loading, showcasing nearly 2.7 times higher than the reference. Compared to random generation methods, the BO approach significantly enhances optimization efficiency by balancing exploration and exploitation to improve the recoverable hinge-like strain capacity in ACCC energy harvesters. Furthermore, the learning-driven framework proactively identifies and eliminates cases exhibiting splitting or non-auxetic behavior, further refining the optimization outcomes.

As BO iterations progress to enhance the recoverable hinge-like strain capacity in ACCCs, the joint size increases, the aspect ratio decreases, and the relative densities rise. However, some fluctuations occur due to the exploration phase of BO. These structural modifications, within a specific range, lead to greater crack formation in the ligaments while maintaining non-splitting and auxetic behavior, ultimately improving the objective function for higher recoverable hinge-like strain capacity. The increased recoverable strain enhances strain transfer to the bonded PVDF film, thereby improving the output voltage. Additionally, as BO iterations continue, the value of d_{sp} decreases, resulting in reduced chirality and increased ligament cracking, eventually stabilizing around zero. These findings suggest that avoiding negative d_{sp} values may help mitigate splitting failure in practical geometric design of ACCCs. Furthermore, as BO advances, the stress–strain curves shift upward, showing higher peak stress, while the absolute value of the negative Poisson's ratio decreases. These adjustments, within a controlled range, encourage ligament crack formation while preserving non-splitting and auxetic characteristics, thereby enhancing the recoverable hinge-like strain capacity and energy harvesting performance.

This framework can be further extended for the inverse design of ACCC energy harvesters in various engineering scenarios (Fig. 6f), tailored to specific properties such as specimen sizes, load capacities, and dimensions of the bonded piezoelectric material. The piezoelectric film is bonded to the cementitious matrix using silicone rubber, which serves as an adhesive layer to facilitate strain transfer. However, some strain loss occurs due to larger cracks in the ligaments and partial debonding between the PVDF and silicone rubber. To improve strain transfer from the ligaments to the PVDF, a stronger adhesive material with higher bond strength could be considered in the future study. Fatigue testing will also be further explored in subsequent investigations.

CRediT authorship contribution statement

Jinbao Xie: Writing – review & editing, Writing – original draft, Visualization, Validation, Software, Methodology, Investigation, Formal analysis, Data curation, Conceptualization. **Yading Xu:** Writing – review & editing, Formal analysis, Conceptualization. **Zhaozheng Meng:** Writing – review & editing, Software. **Minfei Liang:** Writing – review & editing, Methodology. **Wen Zhou:** Writing – review & editing, Methodology. **Yubao Zhou:** Writing – review & editing, Validation. **Chen Liu:** Writing – review & editing, Visualization. **Erik Schlangen:** Writing – review & editing, Supervision, Resources. **Branko Šavija:** Writing – review & editing, Validation, Supervision, Resources, Project administration, Methodology, Funding acquisition, Conceptualization.

Declaration of competing interest

The authors declare that they have no known competing financial interests or personal relationships that could have appeared to influence the work reported in this paper.

Acknowledgements

Jinbao Xie, Minfei Liang, Yubao Zhou, Chen Liu would like to acknowledge the funding supported by China Scholarship Council (CSC) under the grant CSC No. 202006260045, 202007000027, 202006260051, 201906950102. The experimental part of the study was funded by the Dutch Research Council (NWO) through the Open Mind Project "Auxetic Concrete Energy Harvester", grant number 18764. Yading Xu, Zhaozheng Meng, Wen Zhou, Branko Šavija acknowledge the financial support of the European Research Council (ERC) within the framework of the ERC Starting Grant Project "Auxetic Cementitious Composites by 3D printing (ACC-3D)", Grant Agreement Number 101041342. Views and opinions expressed are however those of the author(s) only and do not necessarily reflect those of the European Union or the European Research Council. Neither the European Union nor the granting authority can be held responsible for them.

Appendix A. Supplementary data

Supplementary data to this article can be found online at https://doi.org/10.1016/j.matdes.2026.115745.

Data availability

Data will be made available on request. The model code used to implement the learning-driven computational framework in this study has been deposited in the public repository Zenodo at 10.5281/zenodo.15460690. The codes that support the findings of this study are available from the corresponding author upon request.

References

[1] S.R. Anton, H.A. Sodano, A review of power harvesting using piezoelectric materials (2003–2006), Smart Mater. Struct. 16 (2007) R1–R21.
[2] M. Safaei, H.A. Sodano, S.R. Anton, A review of energy harvesting using piezoelectric materials: state-of-the-art a decade later (2008–2018), Smart Mater. Struct. 28 (2019) 113001.
[3] W. Dong, S. Gao, S. Peng, L. Shi, S.P. Shah, W. Li, Graphene reinforced cement-based triboelectric nanogenerator for efficient energy harvesting in civil infrastructure, Nano Energy 131 (2024) 110380.
[4] G. Zhu, Z.-H. Lin, Q. Jing, P. Bai, C. Pan, Y. Yang, Y. Zhou, Z.L. Wang, Toward large-scale energy harvesting by a nanoparticle-enhanced triboelectric nanogenerator, Nano Lett. 13 (2013) 847–853.
[5] W. Dong, C. Zhao, S. Peng, C. Wu, T. Kim, K. Wang, W. Li, Recycled carbon fibre/cement-based triboelectric nanogenerators toward energy-efficient and smart civil infrastructure, Compos. B Eng. 303 (2025) 112603.
[6] P. Cahill, N. Nuallain Nora Aine, N. Jackson, A. Mathewson, R. Karoumi, V. Pakrashi, Energy harvesting from train-induced response in bridges, J. Bridg. Eng. 19 (2014) 04014034.
[7] Y.-F. Su, R.R. Kotian, N. Lu, Energy harvesting potential of bendable concrete using polymer based piezoelectric generator, Compos. B Eng. 153 (2018) 124–129.
[8] J. Xie, Y. Xu, Z. Wan, A. Ghaderiaram, E. Schlangen, B. Šavija, Modelling of energy harvesting with bendable concrete and surface-mounted PVDF, Smart Mater. Struct. 33 (2024) 085008.
[9] V.C. Li, On engineered cementitious composites (ECC) a review of the material and its applications, J. Adv. Concr. Technol. 1 (2003) 215–230.
[10] Q.-H. Li, A.-M. Luo, B.-T. Huang, G.-Z. Wang, S.-L. Xu, Bond behavior between steel bar and strain-hardening fiber-reinforced cementitious composites under fatigue loading, Eng. Struct. 314 (2024) 118354.
[11] E.-H. Yang, V.C. Li, Tailoring engineered cementitious composites for impact resistance, Cem. Concr. Res. 42 (2012) 1066–1071.
[12] D. Gu, J. Pan, M. Luković, Understanding shear-resisting mechanism in reinforced engineered cementitious composite (ECC) beams using distributed strain measurements, Eng. Struct. 327 (2025) 119612.
[13] M. Moini, J. Olek, J.P. Youngblood, B. Magee, P.D. Zavattieri, Additive manufacturing and performance of architectured cement-based materials, Adv. Mater. 30 (2018) 1802123.
[14] M. Posani, V. Voney, P. Odaglia, Y. Du, A. Komkova, C. Brumaud, B. Dillenburger, G. Habert, Low-carbon indoor humidity regulation via 3D-printed superhygroscopic building components, Nat. Commun. 16 (2025) 425.
[15] S. Gupta, R. Moini, Tough cortical bone-inspired tubular architected cement-based material with disorder, Adv. Mater. 36 (2024) 2313904.
[16] A. Prihar, S. Gupta, H.S. Esmaeeli, R. Moini, Tough double-bouligand architected concrete enabled by robotic additive manufacturing, Nat. Commun. 15 (2024) 7498.
[17] Y. Xu, H. Zhang, E. Schlangen, M. Luković, B. Šavija, Cementitious cellular composites with auxetic behavior, Cem. Concr. Compos. 111 (2020) 103624.
[18] Y. Xu, E. Schlangen, M. Luković, B. Šavija, Tunable mechanical behavior of auxetic cementitious cellular composites (CCCs): experiments and simulations, Constr. Build. Mater. 266 (2021) 121388.
[19] J. Xie, Y. Xu, Z. Wan, A. Ghaderiaram, E. Schlangen, B. Šavija, Auxetic cementitious cellular composite (ACCC) PVDF-based energy harvester, Energ. Buildings 298 (2023) 113582.
[20] J. Xie, Y. Xu, Z. Meng, M. Liang, Z. Wan, B. Šavija, Peanut shaped auxetic cementitious cellular composite (ACCC), Constr. Build. Mater. 419 (2024) 135539.
[21] M. Chen, S. Fang, G. Wang, Y. Xuan, D. Gao, M. Zhang, Compressive and flexural behaviour of engineered cementitious composites based auxetic structures: an experimental and numerical study, J. Build. Eng. 86 (2024) 108999.
[22] D. Valverde-Burneo, N. García-Troncoso, I. Segura, M. García-Laborda, Multifunctional cementitious composite: conductive and auxetic behavior, Case Stud. Constr. Mater. 20 (2024) e03358.
[23] X. Ren, R. Das, P. Tran, T.D. Ngo, Y.M. Xie, Auxetic metamaterials and structures: a review, Smart Mater. Struct. 27 (2018) 023001.
[24] S. Song, Z. Ge, J. Liu, K. Sun, S. Zhou, H. Song, H. Zhang, Auxetic cementitious-silicone cellular composite structure with enhanced energy absorption properties, Int. J. Mech. Sci. 111119 (2025).
[25] Z. Cheng, J. Kang, P. Zhu, P. Wang, H. Feng, Three-dimensional rotating rigid-body structure fabricated with engineered cementitious composites for enhanced auxetic behavior and energy absorption, Cem. Concr. Compos. 164 (2025) 106300.
[26] D. Valverde-Burneo, N. García-Troncoso, I. Segura, Influence of material and design parameters on the mechanical performance and specific energy absorption of auxetic HPCC, Constr. Build. Mater. 505 (2025) 144778.
[27] X. Fang, D. Yu, J. Wen, Y. Dai, M.R. Begley, H. Gao, P. Gumbsch, Large recoverable elastic energy in chiral metamaterials via twist buckling, Nature (2025).
[28] J. Xie, S. He, Y. Xu, Z. Meng, W. Zhou, E. Schlangen, B. Šavija, Enhanced elastomer-like auxetic cementitious materials through strain-hardening cementitious composites (SHCC) with extended softening properties, Cem. Concr. Compos. 161 (2025) 106069.
[29] M.H. Fatahi, M. Hamedi, M. Safarabadi, Fabrication and optimal design of a mechanical piezoelectric energy harvester with re-entrant honeycomb substrate for maximizing voltage output, Int. J. Precis. Eng. Manuf. 25 (2024) 335–347.
[30] M.H. Fatahi, M. Hamedi, M. Safarabadi, Experimental and numerical implementation of auxetic substrate for enhancing voltage of piezoelectric sandwich beam harvester, Mech. Adv. Mater. Struct. 29 (2022) 6107–6117.
[31] Z. Meng, Y. Xu, W. Zhou, J. Xie, B. Šavija, Foamed cementitious composites with 3D-printed auxetic lattice reinforcement: enhancing static and cyclic performance, Compos. B Eng. 303 (2025) 112614.
[32] Z. Meng, Y. Xu, J. Xie, W. Zhou, R.J.M. Bol, Q.-F. Liu, B. Šavija, Unraveling the reinforcing mechanisms for cementitious composites with 3D printed multidirectional auxetic lattices using X-ray computed tomography, Mater. Des. 246 (2024) 113331.
[33] W. Zhou, R.J.M. Bol, Y. Zhou, Z. Meng, Y. Xu, J. Xie, B. Šavija, Reinforcing mechanism of lattice-reinforced cementitious composites: insights into flexural performance and material interactions, Mater. Des. 256 (2025) 114332.
[34] M. Hajsadeghi, L. Wan, E.O. Momoh, A. Jayasinghe, R. Vinai, P. Kripakaran, K. E. Evans, J.J. Orr, Compressive behaviour of mortar panels reinforced with polymeric auxetic lattices: experimental testing and numerical modelling, Constr. Build. Mater. 503 (2025) 144585.
[35] A. Jayasinghe, M. Hajsadeghi, L. Wan, J. Orr, R. Vinai, P. Kripakaran, K. Evans, Design and construction of concrete shells using semi-flexible auxetic grids as formwork, Structures 80 (2025) 109833.
[36] M. Chen, X. Yao, L. Zhu, M. Yin, Y. Xiong, N. Hu, Geometric design and performance of single and dual-printed lattice-reinforced cementitious composite, Cem. Concr. Compos. 143 (2023) 105266.
[37] M. Chen, Z. Chen, Y. Xuan, T. Zhang, M. Zhang, Static and dynamic compressive behaviour of 3D printed auxetic lattice reinforced ultra-high performance concrete, Cem. Concr. Compos. 139 (2023) 105046.
[38] R. Ghasemi, M. Safarabadi, M. Haghighi-Yazdi, A. Mirdehghan, Textile-reinforced mortars; an experimental comparative study of tensile strength improvement methods, Proc. Inst. Mech. Eng., Part L: J. Mater.: Desig. Appl. 236 (2022) 1094–1107.
[39] R. Ghasemi, M. Safarabadi, M. Haghighi-Yazdi, S.A. Mirdehghan, Experimental and analytical study of flexural creep of impregnated woven fabric-reinforced concrete, Compos. Struct. 321 (2023) 117192.
[40] Z. Wan, Z. Chang, Y. Xu, B. Šavija, Optimization of vascular structure of self-healing concrete using deep neural network (DNN), Constr. Build. Mater. 364 (2023) 129955.
[41] M. Ohno, M. Pierre, K. Imagawa, T. Ishida, Simulation and learning-driven design for architected cement-based materials, J. Build. Eng. 65 (2023) 105768.
[42] S. Feng, H. Zhou, H. Dong, Using deep neural network with small dataset to predict material defects, Mater. Des. 162 (2019) 300–310.
[43] W. Ma, F. Cheng, Y. Liu, Deep-learning-enabled on-demand design of chiral metamaterials, ACS Nano 12 (2018) 6326–6334.
[44] Z. Zhang, G.X. Gu, Finite-element-based deep-learning model for deformation behavior of digital materials, Adv. Theor. Simul. 3 (2020) 2000031.
[45] G.A. Lyngdoh, N.-K. Kelter, S. Doner, N.M.A. Krishnan, S. Das, Elucidating the auxetic behavior of cementitious cellular composites using finite element analysis and interpretable machine learning, Mater. Des. 213 (2022) 110341.
[46] D. Chen, M. Skouras, B. Zhu, W. Matusik, Computational discovery of extremal microstructure families, Sci. Adv., 4 eaao7005.

[47] M.A. Bessa, P. Glowacki, M. Houlder, Bayesian machine learning in metamaterial design: fragile becomes supercompressible, Adv. Mater. 31 (2019) 1904845.
[48] F. Ahmed, N. Mohammed, H. Mewada, M.S.A. Aziz, C.Y. Khor, An experimental evaluation, performance analysis, and improvement of water desalination system using optimized machine learning, Process Integr. Optim. Sustainability (2025).
[49] F. Ahmed, M.S. Abdul Aziz, F. Shaik, C.Y. Khor, Experimental and numerical investigation of an innovative desalination unit under laminar, transient, and turbulent flow conditions, Chem. Eng. Res. Des. 208 (2024) 683–694.
[50] Y. Cao, F. Su, M.F. Antwi-Afari, J. Lei, X. Wu, Y. Liu, Enhancing mix proportion design of low carbon concrete for shield segment using a combination of Bayesian optimization-NGBoost and NSGA-III algorithm, J. Clean. Prod. 465 (2024) 142746.
[51] C.B. Arachchilage, J. Zhao, N. Dushyantha, W.V. Liu, A transformer-based machine learning model for optimizing the design of cementitious mixtures with mine tailings as supplementary cementitious materials, Cem. Concr. Compos. 165 (2026) 106363.
[52] M.R. Hajighasemi, M. Safarabadi, A. Sheidaei, M. Baghani, M. Baniassadi, Design and manufacture of a smart macro-structure with changeable effective stiffness, Int. J. Appl. Mech. 12 (2020) 2050001.
[53] M.E. Scyphers, J.E.C. Missik, H. Kujawa, J.A. Paulson, G. Bohrer, Bayesian optimization for anything (BOA): an open-source framework for accessible, user-friendly Bayesian optimization, Environ. Model. Software 182 (2024) 106191.
[54] M. Liang, Z. Li, S. He, Z. Chang, Y. Gan, E. Schlangen, B. Šavija, Stress evolution in restrained GGBFS concrete due to autogenous deformation: Bayesian optimization of aging creep, Constr. Build. Mater. 324 (2022) 126690.
[55] B. Hu, Z. Wang, C. Du, W. Zou, W. Wu, J. Tang, J. Ai, H. Zhou, R. Chen, B. Shan, Multi-objective Bayesian optimization accelerated design of TPMS structures, Int. J. Mech. Sci. 244 (2023) 108085.
[56] S. Kang, H. Moon, S. Shin, M. Mousavi, H. Sung, S. Ryu, Design of auxetic metamaterial for enhanced low cycle fatigue life and negative Poisson's ratio through multi-objective Bayesian optimization, Mater. Des. 252 (2025) 113798.
[57] J. Du, H. Ma, D. Sun, P. Pan, Data driven strength and strain enhancement model for FRP confined concrete using Bayesian optimization, Structures 41 (2022) 1345–1358.
[58] P. Guo, W. Meng, Y. Bao, Knowledge-guided data-driven design of ultra-high-performance geopolymer (UHPG), Cem. Concr. Compos. 153 (2024) 105723.
[59] Z. Vangelatos, H.M. Sheikh, P.S. Marcus, C.P. Grigoropoulos, V.Z. Lopez, G. Flamourakis, M. Farsari, Strength through defects: a novel Bayesian approach for the optimization of architected materials, Sci. Adv., 7 eabk2218.
[60] I. Kuszczak, F.I. Azam, M.A. Bessa, P.J. Tan, F. Bosi, Bayesian optimisation of hexagonal honeycomb metamaterial, Extreme Mech. Lett. 64 (2023) 102078.
[61] J.W. Sohn, J. Jeon, S.B. Choi, An investigation on dynamic signals of MFC and PVDF sensors: experimental work, Adv. Mech. Eng., (2013).
[62] H.-H. Huang, K.-S. Chen, Design, analysis, and experimental studies of a novel PVDF-based piezoelectric energy harvester with beating mechanisms, Sens. Actuators, A 238 (2016) 317–328.
[63] S. Daulton, M. Balandat, E.J.A.i.N.I.P.S. Bakshy, Parallel bayesian optimization of multiple noisy objectives with expected hypervolume improvement, 34 (2021) 2187-2200.
[64] S. Daulton, M. Balandat, E.J.A.i.N.I.P.S. Bakshy, Differentiable expected hypervolume improvement for parallel multi-objective Bayesian optimization, 33 (2020) 9851-9864.
[65] D.R. Jones, M. Schonlau, W.J. Welch, Efficient global optimization of expensive black-box functions, J. Glob. Optim. 13 (1998) 455–492.